Applied Catalysis B: Environmental 95 (2010) 423–429

Contents lists available at ScienceDirect

Applied Catalysis B: Environmental

journal homepage: www.elsevier.com/locate/apcatb

Self-assembled hematite (α-Fe_2O_3) nanotube arrays for photoelectrocatalytic degradation of azo dye under simulated solar light irradiation

Zhonghai Zhang [a], Md. Faruk Hossain [b], Takakazu Takahashi [a,*]

[a] Graduate School of Science and Engineering for Research, University of Toyama, 3190 Gofuku, Toyama 930-8555, Toyama, Japan
[b] Graduate School of Science and Engineering for Education, University of Toyama, 3190 Gofuku, Toyama 930-8555, Toyama, Japan

ARTICLE INFO

Article history:
Received 8 November 2009
Received in revised form 14 January 2010
Accepted 20 January 2010
Available online 25 January 2010

Keywords:
Hematite (α-Fe_2O_3)
Anodization
Nanotubes
Photoelectrochemical
Photoelectrocatalytic

ABSTRACT

Self-assembly aligned hematite (α-Fe_2O_3) nanotube arrays (α-Fe_2O_3 NTs) were successfully prepared on the Fe foils by a simple two-step electrochemical anodization method in NH_4F organic electrolyte. The α-Fe_2O_3 NTs electrodes were characterized by field-emission scanning electron microscopy, energy dispersive X-ray spectroscopy, grazing incidence X-ray diffraction, UV–vis absorbance spectra, and X-ray photoelectron spectroscopy. The resulting α-Fe_2O_3 NTs showed a pore diameter of 40 nm, thickness of 2 μm, and a minimum wall thickness of $\sim$10 nm. The systematic photoelectrochemical responses on the α-Fe_2O_3 NTs electrodes were presented. The maximum photoconversion efficiencies of 0.51% and 0.60% were collected at 0.3 V under illumination of visible light and simulated solar light (AM 1.5G), respectively. The photoelectrocatalytic (PEC) and photocatalytic (PC) activities of the α-Fe_2O_3 NTs electrodes were evaluated by degradation of azo dye. The significant PEC and PC performance indicated that the α-Fe_2O_3 NTs electrodes were an effective photoelectrode under visible light and simulated solar light illumination.

1. Introduction

In recent decades, photocatalytic (PC) technology has received significant attention for hydrogen generation by photoelectrochemical water splitting and decomposition of harmful organic contaminants [1–6]. Since Fujishima and Honda first reported TiO_2 as photoanode for the photoelectrolysis of water [7], the TiO_2 materials have been widely researched for PC application. Whereas, the wide band gap ($\sim$3.2 eV) of TiO_2 material limits its practical application because it only can be excited with light of wavelength near or shorter than 385 nm. The primary scientific and technological objective has been focused on exploring novel photocatalysts with high efficiency of utilization of solar irradiation, narrow band gap, operational stability, and preparation with relatively low cost [8]. Iron oxide (α-Fe_2O_3, hematite) is one of promising candidates for PC application due to its narrow band gap about 2.0–2.2 eV, which absorbs light up to 600 nm, collects up 40% of the solar spectrum energy, stability in most aqueous solution (pH > 3) and it maybe one of the cheapest semiconductor materials [9–11]. However, the drawbacks of α-Fe_2O_3 materials, such as poor electron mobility, generally in the range of 0.01 $cm^2/V\,s^4$ to 0.1 $cm^2/V\,s^4$, which results the high electron–hole recombination rate, and short hole diffusion length (2–4 nm), are the major challenger for its practical application [12]. Recently, nanostructuring techniques have been proven useful in increasing the performance of α-Fe_2O_3 for photoresponse [13]. The aligned nanotube has been considered the most suitable way to achieve larger enhancement of surface area without an increase of the geometric area, reduced the scattering of free electrons, and enhanced the electrons mobility, which could be expected to achieve higher PC activities.

A variety of fabrication methods such as biomacromolecules template [14], AAO template [15,16], hydrothermal [17], surfactant-assisted solution method [18], and electrochemical anodization [19] have been used for the preparation of α-Fe_2O_3 nanotubes (α-Fe_2O_3 NTs). Among them, electrochemical anodization method shows advantages of easily controllable pore size, good uniformity, and conformability over large areas at low coat.

Because of significant photoelectrochemical performance, the formation of α-Fe_2O_3 NTs with high surface area has been paid much interest by a number of researchers. Misra and co-workers [20] have first fabricated ultrathin α-Fe_2O_3 nanotubes by sonoelectrochemical anodization method for water photooxidation. Grimes and co-workers [21] have discussed temperature dependent growth of α-Fe_2O_3 NTs by anodization method and prepared this nanomaterial at high temperature. However, to our best knowledge, there has been no report regarding application of

* Corresponding author. Tel.: +81 76 445 6716; fax: +81 76 445 6716.
E-mail addresses: zhonghaizhangwill@gmail.com (Z. Zhang), takahash@eng.u-toyama.ac.jp (T. Takahashi).

0926-3373/$ – see front matter © 2010 Elsevier B.V. All rights reserved.
doi:10.1016/j.apcatb.2010.01.022

the α-Fe_2O_3 NTs electrode in the degradation of organic pollutants in photoelectrocatalytic (PEC) process. In this paper, we prepared α-Fe_2O_3 nanotube arrays electrodes in a simple two-step anodization method in room temperature, and studied the PC and PEC performance for degradation of azo dye, such as methylene blue (MB) under illumination of visible light and simulated solar light (AM 1.5 G). MB is commonly considered as a representative organic dye in textile effluents, and it can easily be monitored by optical absorption spectroscopy [22]. Herein, MB is chosen as model contaminants to evaluate the PC and PEC activities of the α-Fe_2O_3 NTs due to its stability under visible light and near UV light.

2. Experimental section

2.1. Materials

Pure iron foils (99.99% purity, 0.2 mm thick) were purchased from Nilaco Corp., Japan. Ethylene glycol (EG), ammonium fluoride (NH_4F), methylene blue, sodium sulfate and ethanol of analytical grade were obtained from Wako Chemicals (Japan) without further purification. All solutions were prepared with doubly distilled deionized water.

2.2. Fabrication of α-Fe_2O_3 nanotube arrays electrode

A two-step electrochemical anodization method was used to fabricate the aligned α-Fe_2O_3 NTs electrode. Prior to anodization, the iron foils (10 mm × 25 mm) were first degreased by sonicating in ethanol and cold distilled water in turn, followed by drying in pure nitrogen stream. The anodization experiments were carried out in a conventional two-electrode system with Fe foil as anode and Pt foil as cathode. The time-dependent current behavior under constant potential was recorded using a computer controlled Keithley 2400 sourcemeter. All electrolytes consisted of 0.3 wt% NH_4F in an aqueous EG solution (2 vol% water in EG).

In the first anodization process, the Fe foil was anodized at 50 V for 5 min, and then the grown nanoporous oxide layer was removed by ultrasonic irradiation in deionized water in 10 min,

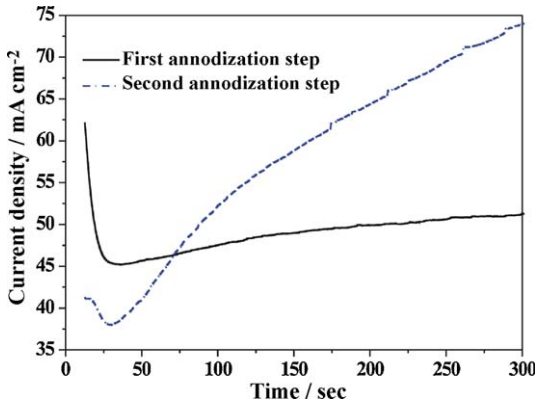

Fig. 1. Constant voltage current density of iron foil anodized in electrolyte containing ethylene glycol +0.3 wt% NH_4F +2.0% water. First-step and second-step, anodized at 50 V and 60 V, respectively.

while the barrier oxide layer of Fe_2O_3 films with ordered hexagonal structures were left on the Fe surface as imprints. The pretreated Fe was used as anode again for the second-step anodization at 50 V for 5 min and aligned and ordered nanotubes arrays were formed. After the electrochemical anodization process, the anodized samples were properly washed with distilled water, and dried in nitrogen stream. All the α-Fe_2O_3 NTs samples were crystallized by annealing in a muffle furnace (TMF5, Thomas) under an oxygen atmosphere at 400 °C for 1 h with heating and cooling rate of 2 °C/min.

2.3. Characterization of α-Fe_2O_3 nanotube arrays electrode

The surface morphologies of α-Fe_2O_3 nanostructures were characterized by field-emission scanning electron microscopy (FE-SEM) (JEOL, FE-SEM 6700) with accelerated voltage of 3 keV, and the elemental composition was estimated by energy-dispersive X-ray spectroscopy (EDS, JED-2200, fitted to the JEOL FE-SEM 6700) analysis. The crystalline structures of the α-Fe_2O_3 NTs samples were characterized by grazing incidence X-ray diffraction (GIXRD) using a diffractometer with Cu Kα radiation (Shimadzu XRD-6000),

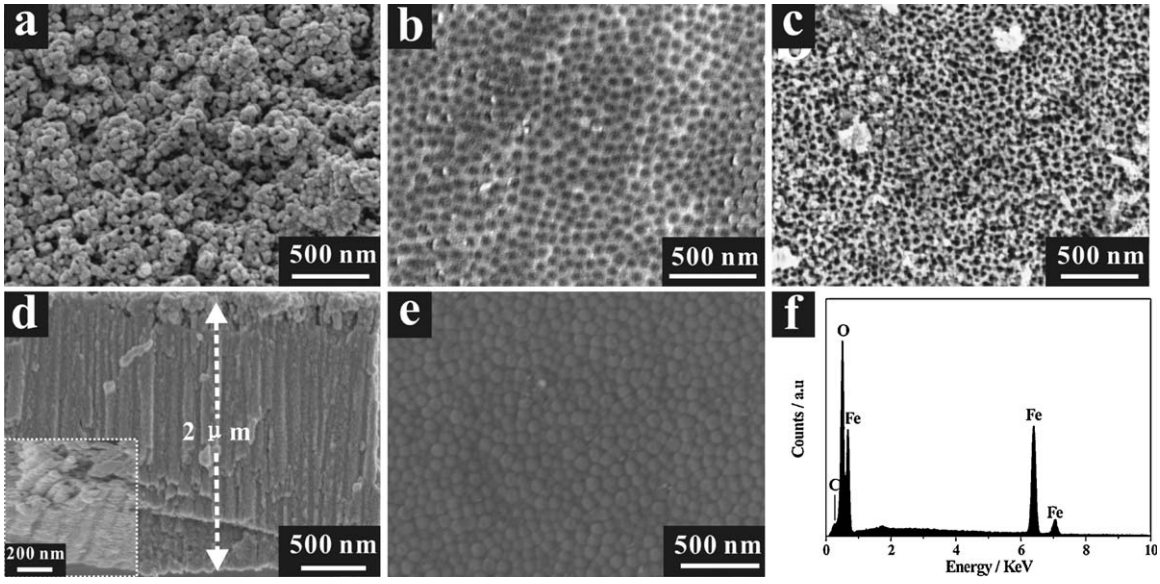

Fig. 2. FE-SEM images of (a) top view of nanoporous α-Fe_2O_3; (b) Fe foil surface with imprints after ultrasonic treatment; (c) top view of α-Fe_2O_3 NTs; (d) cross-sectional image of α-Fe_2O_3 NTs, inset is a high-magnification cross-sectional image; (e) bottom side of the α-Fe_2O_3 NTs that shed from the Fe foil; (f) representative EDS pattern of the α-Fe_2O_3 NTs.

λ = 0.154 nm in the range of 2θ = 20–70°, with scan rate of 4°/min. The UV–visible absorbance spectra of the α-Fe_2O_3 NTs samples were measured using a Jasco V-550 UV–vis spectrophotometer in combination with a single reflection internal accessory (SLM 468, Jasco Corp.). Surface composition of α-Fe_2O_3 NTs was detected using X-ray photoelectron spectroscopy (XPS) (ESCA Lab 220i) with a monochromatic Al anode X-ray gun.

2.4. Photoelectrocatalytic degradation experiments

The PEC degradation experiments were carried out in a Pyrex reactor. Photocurrent was measured in a standard three-electrode configuration with α-Fe_2O_3 NTs electrode as working electrode, Ag/AgCl in saturated KCl as reference electrode, and platinum foil as counter electrode, respectively. The potential was swept linearly at a scan rate of 5 mV s^{-1} between −0.4 V and 0.7 V. All the potentials were referred to Ag/AgCl electrode unless otherwise stated in this paper. The samples were illuminated by an artificial sunlight simulator, consisting of a SOLAX lamp (model: SET-140F, SERIC Ltd.) and an AM 1.5 G filter (100 mW cm^{-2}, thermopile detector from Hamamatsu was used for the measurements). The visible light ($\lambda \geq 420$ nm) PEC performance was carried out by using a band-pass filter in combination with an AM 1.5 filter. The α-Fe_2O_3 NTs electrode was illuminated in an active area of 1.0 cm^{-2}. In addition, 0.01 M sodium sulfate solution was used as supporting electrolyte. MB aqueous solution with initial concentration of 1×10^{-6} M was used in the PEC and PC degradation reaction, and the pH value of the solution was not controlled during the reaction. The concentration of MB solutions were determined by measuring the maximum absorbance at λ = 665 nm.

3. Results and discussion

3.1. Processes of anodization

The two-step real-time constant voltage electrochemical anodization behavior on Fe foils was shown in Fig. 1. In the first step anodization process, the sharp drop of the current behavior in the first 30 s was due to the formation of initial oxide layer, followed by an increase in current due to the oxide layer pitting by the fluoride ions, and the current gradually increased. In the second-step anodization process, in the first 30 s, the decreased current is much lower than that in first step, and then the current dramatically increased, indicating the fast growth process of α-Fe_2O_3 NTs. The first-step anodization was actually a pretreatment for formation of well-ordered nanoporous template for the second-step anodization growth of nanotubes.

3.2. Morphology of α-Fe_2O_3 nanotubes

The FE-SEM images and EDS pattern of the as-prepared α-Fe_2O_3 NTs were illustrated in Fig. 2. Fig. 2a showed the top view of the samples in the first-step anodization, and a nanoporous structure was formed. The pores diameter was small, the wall thickness was high, and the surface was rough. After the ultrasonic treatment, ordered imprints were left on the Fe surface (Fig. 2b) with a regular hexagon-shaped structure, and acted as a template for the second-step anodization. The FE-SEM images of top view, cross-sectional and bottom side images after second-step anodization were shown in Fig. 2c–e, respectively. The surface morphology demonstrated a nanotubular structure with an average pore diameter of 40 nm, thin wall thickness of ~10 nm, and length of 2 μm. The bottom side of the nanotubes showed an approximate 6-fold symmetry, all tubes assumed a rough hexagonal shape, and each nanotube was surrounded by 6 closest neighboring ones. The preparation of α-Fe_2O_3 NTs were further demonstrated by the elemental signature

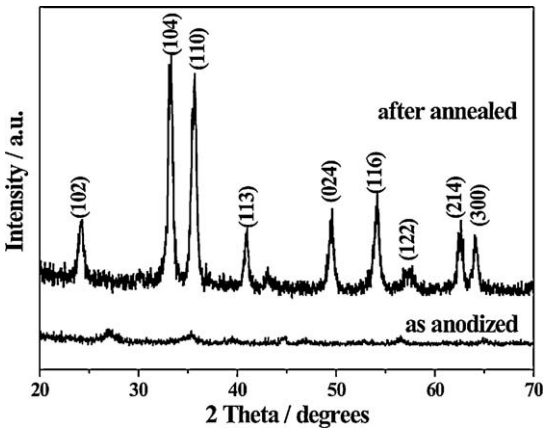

Fig. 3. GIXRD patterns of α-Fe_2O_3 nanotube arrays electrode before and after annealed at 400 °C for 1 h.

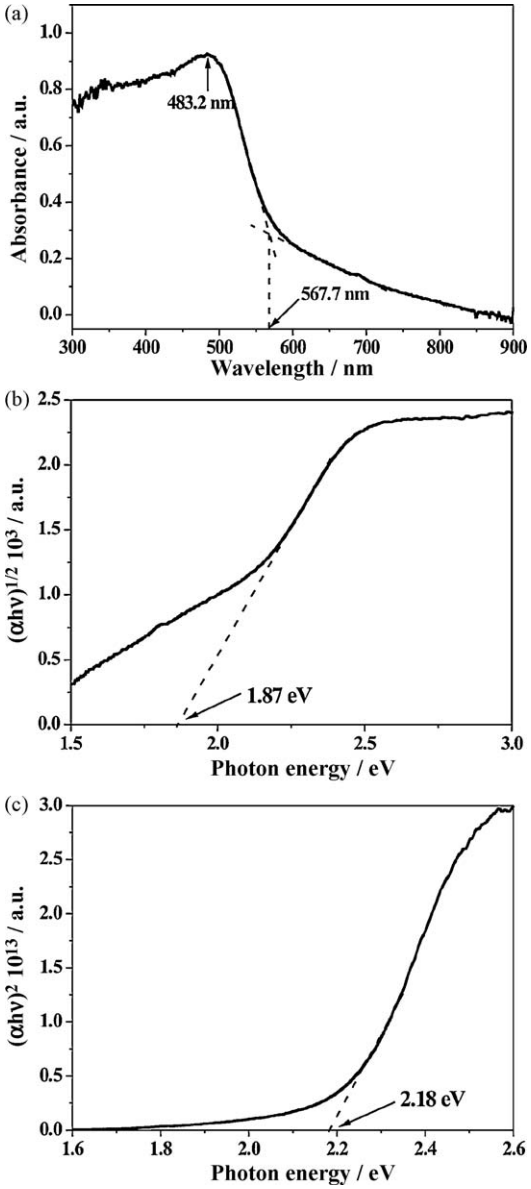

Fig. 4. (a)UV–vis absorbance spectrum of α-Fe_2O_3 NTs electrode. Tauc plot analysis of optical band gap of (b) indirect transition, and (c) direct transition for α-Fe_2O_3 NTs electrode.

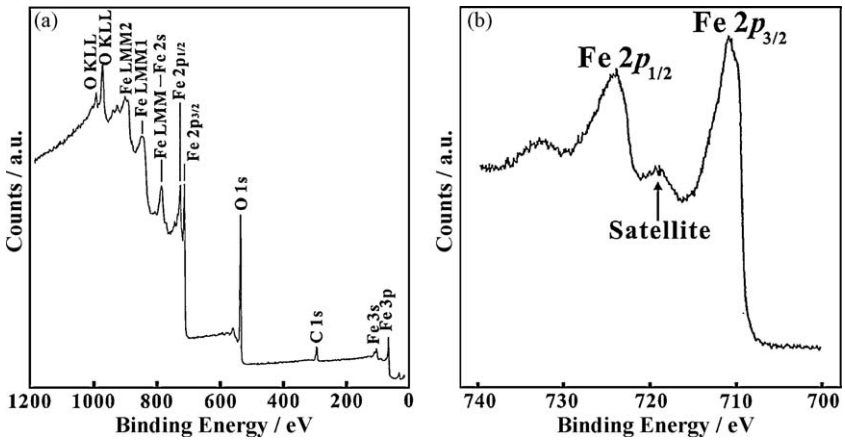

Fig. 5. (a) XPS spectrum of α-Fe_2O_3 NTs sample; (b) high-resolution XPS spectrum of Fe 2p.

in the EDS spectrum (Fig. 2f). The EDS spectrum showed existence of Fe and O with atomic ratios of 38.67% and 52.74%.

3.3. XRD analysis

GIXRD was performed on the as-anodized and annealed α-Fe_2O_3 NTs samples. The GIXRD peak patterns were shown in Fig. 3. The as-anodized Fe_2O_3 NTs were amorphous in nature and then were converted to crystalline structure after annealing at 400 °C in an oxygen atmosphere for 1 h. All the peaks of the annealed sample can be well indexed to a pure rhombohedral symmetry of Fe_2O_3 (space group: $R3c(167)$, $a = 0.5035$, $b = 0.5035$, $c = 1.3748$ nm; JCPDS card No. 33-0664) indicating the crystalline hematite phase. No other peaks for impurities, such as γ-Fe_2O_3 and Fe_3O_4, were observed. The diffraction peaks were strong and sharp, which indicated good crystallization.

3.4. UV–vis absorbance analysis

The α-Fe_2O_3 NTs samples were reddish brown in color, and the optical absorption spectrum was shown in Fig. 4a. The maximum absorption wavelength was around 483.2 nm, and the band gap absorption edge was around 567.7 nm. The optical absorption in α-Fe_2O_3 films were most attributed to indirect transition, while some groups have reported the evidence for direct transition [23–25]. A direct charger transition causes the absorption in UV region, corresponding to the ligand-metal transfer from O^{2-} 2p → Fe^{3+} 3d, and an indirect charger transition causes the absorption in visible

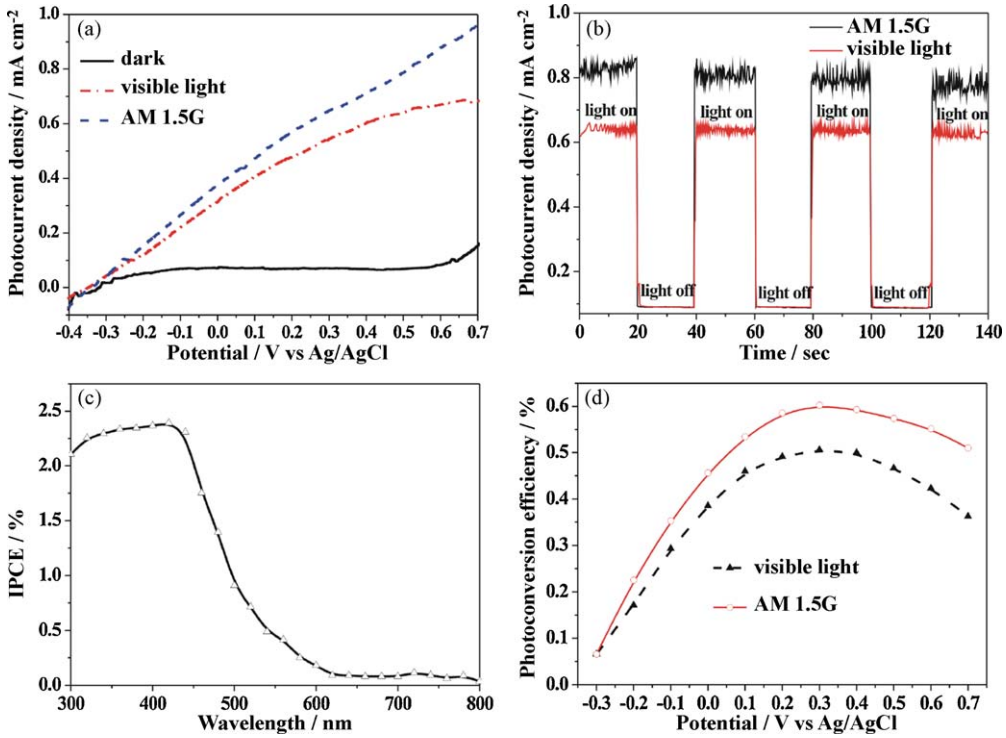

Fig. 6. (a) Linear sweep voltammagrams of α-Fe_2O_3 NTs electrodes in dark, illuminated under visible and simulated solar light in a scan rate of 5 mV/s; (b) Amperometric *I–t* curves of the α-Fe_2O_3 NTs electrode at an applied voltage of +0.6 V with 20 s visible light and simulated solar light on/off cycles; (c) IPCE spectrum on α-Fe_2O_3 NTs electrode at an applied voltage of +0.6 V; (d) Photoconversion efficiency on α-Fe_2O_3 NTs electrode as a function of applied potential.

Table 1
The values of rate constant k and regression coefficients (R) of MB degradation in different processes.

Processes	PEC AM 1.5 G	PEC visible light	PC AM 1.5 G	PC visible light	DP	EO
Rate constant (min^{-1})	0.063	0.0479	0.0200	0.0160	0.0009	0.0001
R	0.9882	0.9859	0.9996	0.9967	0.9967	0.9907

light region, corresponding to the metal-metal transfer of $2Fe^{3+} \rightarrow Fe^{2+} + Fe^{4+}$ [26]. From the Tauc plot analysis (as shown in Fig. 4b and c), the indirect transition and direct transition band gap of 1.87 eV and 2.18 eV were estimated, respectively. This was in accordance with the band gap of hematite, and agrees well with the preciously reported results [27–29].

3.5. XPS analysis

The XPS spectra were recorded to determine the chemical components and the oxidation states of Fe at the surface of the α-Fe_2O_3 NTs sample, as shown in Fig. 5. It revealed that the surface of the sample contained Fe, O, and C elements. The residual carbon could originate from the precursor solution and the XPS instrument itself.

Higher resolution spectrum of Fe was shown in Fig. 5b. The spectrum indicated the existence of doublet Fe $2p_{3/2}$ and Fe $2p_{1/2}$ with binding energies of 711 eV and 725 eV, respectively. The Fe $2p_{3/2}$ peak also associated with a satellite peak located approximately 8 eV higher than the main peak of Fe $2p_{3/2}$, which were characteristic of α-Fe_2O_3 and agreed well with the literature values [30].

3.6. Photoelectrochemical properties of α-Fe_2O_3 nanotube array electrode

Systematic electrochemical measurements were carried out to evaluate the photoelectrochemical properties of α-Fe_2O_3 NTs electrode. In comparison to TiO_2, α-Fe_2O_3 is chemically less stable in acidic solution, so we can conduct all the photoelectrochemical studies in a 0.01 M Na_2SO_4 electrolyte solution (pH ~7). Fig. 6a showed a set of linear sweep voltammagrams (LSV) recorded on these α-Fe_2O_3 NTs electrodes in dark and under illumination of visible and simulated solar light. The dark LSV from −0.4 V to +0.6 V showed a very small current, and the current was gradually increased, which implied in no electrochemical oxidation occurring below +0.6 V. Under illumination, significant increase of photocurrent was observed, and the photocurrent was potential dependent, the photocurrent increased as the applied potentials was scanned toward to more positive potential. Significantly, there was no saturation of photocurrent observed in all studied α-Fe_2O_3 NTs electrodes, which indicated efficient charge separation under illumination.

The photoresponse of α-Fe_2O_3 NTs electrode was studied in amperometric I–t curve, as showed in Fig. 6b. The photocurrent collected with light on/off cycles at +0.6 V. The rise and fall of the photocurrent corresponded well to the illumination being switched on and off. The generation of photocurrent consisted of two steps, the first step of the photocurrent appeared promptly after the illumination, the second step of the photocurrent reached a steady state, and this pattern of photocurrent was highly reproducible for numerous on–off cycles of illumination. The photocurrent density of 0.67 mA and 0.88 mA at +0.6 V was achieved under illumination of visible and simulated solar light, respectively, and photocurrent contribution of visible light was calculated to 76%.

The incident-photon-to-current conversion efficiency (IPCE) measurement was carried out to confirm the photoactive wavelength region of α-Fe_2O_3 NTs electrodes. IPCE can be calculated using the following equation [31]:

$$\mathrm{IPCE} = \frac{(1240 \times I)}{(\lambda \times J_{\mathrm{light}})} \quad (1)$$

where I is the photocurrent density, λ is the incident light wavelength, and J_{light} is the measured intensity of incident light. The IPCE measurement was performed at an applied potential of 0.6 V. As seen from Fig. 6c, the IPCE onset around 600 nm coincided with the onset of strong light absorption (Fig. 4a), and then the IPCE value significant increased with the decrease of wavelength, and reached the highest value of 2.4% at 420 nm. This indicated that at

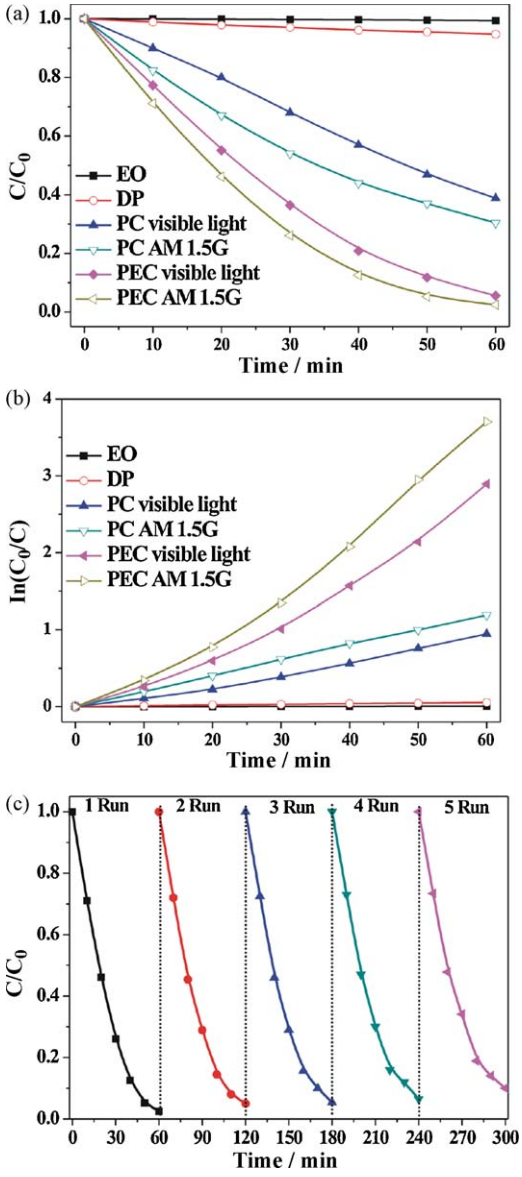

Fig. 7. (a) Different processes of PEC, PC, DP, and EO on MB degradation; (b) Kinetics of different degradation processes; (c) stability of α-Fe_2O_3 NTs electrode under illumination of simulated solar light.

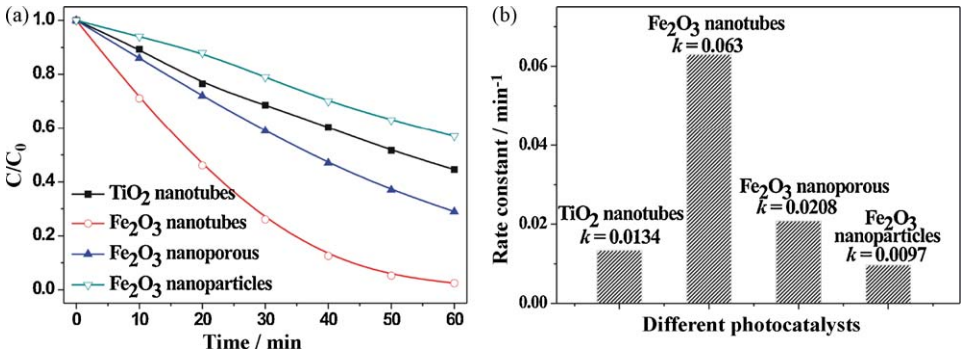

Fig. 8. (a) PEC performance on different photocatalysts; (b) histogram of rate constants (k) on different photocatalysts.

shorter wavelength, the more energetic photons have higher quantum efficiency, which promoted the charge separation. The quickly drop of IPCE value at longer wavelength than 420 nm may be due to the different charge-transfer processes, direct transition and indirect transition, as former discussion.

The photoconversion efficiency of light energy to chemical energy of α-Fe_2O_3 NTs electrode was calculated using the equation [32]:

$$\%\varepsilon = I(1.23 - E_{app}) \times 100/J_{light} \quad (2)$$

where ε is the photoconversion efficiency, I is the photocurrent density (mA cm^{-2}), E_{app} is the value of the applied potential, and J_{light} is the intensity of the incident light. The plot of efficiency versus applied potential showed the maximum efficiency value of 0.51% and 0.60% at +0.3 V under illumination of visible and simulated solar light, respectively, as shown in Fig. 6d. A further reduction of wall thickness of α-Fe_2O_3 NTs and enhancement of crystallinty can be expected to improve the photoconversion efficiency through the reduction of recombination of photogenerated charges.

3.7. PEC degradation of MB under visible and simulated solar light irradiation

The PEC and PC activities of α-Fe_2O_3 NTs electrode were evaluated by studying the degradation of MB in aqueous solution under illumination of visible and simulated solar light. Before the PEC and PC experiments, the samples were put in the MB solution for 1 h and reached the equilibrium. The degradation in different processes, PEC, PC, direct photolysis (DP), and electrochemical oxidation (EO), were summarized in Fig. 7a. Applied bias potential of 0.6 V was used in all PEC and EO processes. It was easily observed that the PEC process under illumination of simulated solar light provided the most powerful way to degrade the MB in aqueous solution. Both in PEC and PC processes, the removal rate under illumination of simulated solar light was higher than that under illumination of visible light. The removal with DP was insignificant, which proved that the MB was stable with near UV and visible light illumination. The result with EO was also in good agreement with the data in Fig. 6a, that the EO was not occurred evidently in this process with the applied potential of 0.6 V. The experimental data of Fig. 7a were found to fit approximately a pseudo-first-order kinetic model by the linear transforms $\ln(C_0/C) = f(t) = kt$ (k is rate constant), as shown in Fig. 7b. The values of the rate constant, k, and regression coefficient were listed in Table 1. In PEC and PC processes, the visible light shows the similar contribution rate of 0.76 and 0.80, which contribution rate was well agreement with the results of visible light photocurrent analysis in Fig. 5.

The stability of a photoelectrode was also important to its practical application for organic pollutants degradation. As shown in Fig. 7c, after five times continuous runs for MB degradation, the samples were rinsed carefully before starting a new test, the α-Fe_2O_3 NTs electrodes did not exhibit any significant loss of activity under illumination of simulated solar light. This good repetition of degradation results was also verified by stable photocurrent, indicating potential application for environmental remediation.

The PEC activities under illumination of simulated solar light of different photocatalysts, α-Fe_2O_3 NTs, α-Fe_2O_3 nanoporous, α-Fe_2O_3 nanoparticles, and TiO_2 NTs, were investigated and showed in Fig. 8a. The α-Fe_2O_3 nanoporous were prepared in one step anodization method, α-Fe_2O_3 nanoparticles with diameter of 100 nm and thickness of 2 μm were prepared in a dip coating method on Fe foil as previous reported [20], and TiO_2 nanotubes with diameter of 80–100 nm and thickness of 2 μm were also prepared in anodization process as previous reported [33]. The α-Fe_2O_3 NTs showed the best PEC performance, as depicted the histogram in Fig. 8b. The rate constant on α-Fe_2O_3 NTs was 4.7 folds higher than that on TiO_2 NTs, which indicated that the α-Fe_2O_3 NTs was an efficient photocatalyst for PEC degradation of azo dye.

4. Conclusions

In summary, the aligned α-Fe_2O_3 NTs electrode was prepared with a simple two-step anodization method. The α-Fe_2O_3 NTs electrode showed an efficient photoelectrochemical properties and excellent PEC and PC activity for azo dye degradation. Further efforts will be focused on obtaining thinner walled NTs for improving the photoconversion efficiency, and then further enhancing the photocatalytic activity.

Acknowledgments

This work was supported in part by a Grant-in-Aid for Scientific Research from the Japan Society for the Promotion of Science (JSPS). Z. Z acknowledges also the support of this work by post-doctoral fellowship from the venture business laboratory of Toyama University.

References

[1] A. Fujishima, T.N. Rao, D.A. Tryk, J. Photochem. Photobiol. C 1 (2000) 1–21.
[2] X.B. Chen, S.S. Mao, Chem. Rev. 107 (2007) 2891–2959.
[3] Z.H. Zhang, Y. Yuan, G.Y. Shi, Y.J. Fang, L.H. Liang, H.C. Ding, L.T. Jin, Environ. Sci. Technol. 41 (2007) 6259–6263.
[4] X.K. Li, N. Kikugawa, J.H. Ye, Adv. Mater. 20 (2008) 3816–3819.
[5] S. Saremi-Yarahmadi, U.K.G. Wijayantha, A.A. Tahir, B. Vaidhyanathan, J. Phys. Chem. C 113 (2009) 4768–4778.
[6] Y.S. Sohn, Y.R. Smith, M. Misra, V. Subramanian, Appl. Catal. B: Environ. 84 (2008) 372–378.
[7] A. Fujishima, K. Honda, Nature 238 (1972) 37–38.
[8] Y.F. Guo, X. Quan, N. Lu, H.M. Zhao, S. Chen, Environ. Sci. Technol. 41 (2007) 4422–4427.

[9] Y.S. Hu, A. Kleiman-Shwarsctein, A.J. Forman, D. Hazen, J.N. Park, E.W. McFarland, Chem. Mater. 20 (2008) 3803–3805.
[10] I. Cesar, A. Kay, J.A.G. Martinez, M. Gratzel, J. Am. Chem. Soc. 128 (2006) 4582–4583.
[11] D.K. Zhong, J.W. Sun, H. Inumaru, D.R. Gamelin, J. Am. Chem. Soc. 131 (2009) 6086–6087.
[12] G.K. Mor, H.E. Prakasam, O.K. Varghese, K. Shankar, C.A. Grimes, Nano Lett. 7 (2007) 2356–2364.
[13] K. Sivula, F.L. Formal, M. Gratzel, Chem. Mater. 21 (2009) 2862–2867.
[14] D.D. Archibald, S. Mann, Nature 364 (1993) 430–433.
[15] J. Chen, L. Xu, W. Li, X. Gou, Adv. Mater. 17 (2005) 582–586.
[16] H.J. Zhou, S.S. Wong, ACS Nano 2 (2008) 944–958.
[17] C.J. Jia, L.D. Sun, Z.G. Yan, L.P. You, F. Luo, X.D. Han, Y.C. Pang, Z. Zhang, C.H. Yan, Angew. Chem. Int. Ed. 44 (2005) 4328–4333.
[18] L. Liu, H.Z. Kou, W.L. Mo, H.J. Liu, Y.Q. Wang, J. Phys. Chem. B 110 (2006) 15218–15223.
[19] H.E. Parkasam, O.K. Varghese, M. Paulose, G.K. Mor, C.A. Grimes, Nanotechnology 17 (2006) 4285–4291.
[20] S.K. Mohapatra, S.E. John, S. Banerjee, M. Misra, Chem. Mater. 21 (2009) 3048–3055.
[21] T.J. LaTempa, X.J. Feng, M. Paulose, C.A. Grimes, J. Phys. Chem. C 113 (2009) 16293.
[22] J. Lin, R.L. Zong, M. Zhou, Y.F. Zhu, Appl. Catal. B: Environ. 89 (2009) 425–431.
[23] A. Duret, M. Gratzel, J. Phys. Chem. B 109 (2005) 17184–17191.
[24] M. Selim, A. Sawaby, Z. El Mandouh, Mater. Res. Bull. 35 (2000) 2123–2133.
[25] N. Beermann, L. Vayssieres, S.E. Lindquist, A. Hagfeldt, J. Electrochem. Soc. 147 (2000) 2456–2461.
[26] A. Kay, I. Cesar, M. Gratzel, J. Am. Chem. Soc. 128 (2006) 15714–15721.
[27] E.L. Miller, D. Paluselli, B. Marsen, R.E. Rocheleau, Thin Solid Films 466 (2004) 307–313.
[28] N. Ozer, F. Tepehan, Sol. Energy Mater. Sol. Cells 56 (1998) 141–152.
[29] S. Khan, J. Akikusa, J. Phys. Chem. B 103 (1999) 7184–7189.
[30] M. Muhler, R. Schlogl, G. Ertl, J. Catal. 138 (1992) 413–444.
[31] A.B. Murphy, P.R.F. Barnes, L.K. Randeniya, I.C. Plumb, I.E. Grey, M.D. Horne, J.A. Glasscock, Int. J. Hydrogen Energy 31 (2006) 1999–2017.
[32] B. Parkinson, Acc. Chem. Res. 17 (1984) 431–437.
[33] M. Paulose, K. Shankar, S. Yoriya, H.E. Prakasam, O.K. Varghese, G.K. Mor, T.A. Latempa, A. Fitzgerald, C.A. Grimes, J. Phys. Chem. B 110 (2006) 16179.